Flapping motion of a permeable flag in uniform flow

doi: 10.1088/1873-7005/aae933

Flapping motion of a permeable flag in uniform flow

Kazutaka Nishiura[1], Yu Nishio[1], Seiichiro Izawa[1] and Yu Fukunishi[1]

[1]Graduate School of Engineering, Tohoku University, 6-6-01 Aramaki-Aoba, Aoba-ku, Sendai 980-8579, Japan

E-mail: vexillologist1870@gmail.com

Abstract. The flapping motion of a permeable square-shaped flag is studied using an incompressible SPH method together with a newly proposed permeable flag model. Wind tunnel experiments are also performed, and the results are compared. The present model is successful in simulating two characteristic states depending on the uniform velocity, namely the "stretched-straight state" and the "flapping state." Both the oscillation periods and the tail-end trajectories quantitatively agree with the experiments. However, the bistable region, which appears in the experiments, is not seen in the computational results. Except for the high-permeability case, the flags oscillate two dimensionally and no flow separation is observed irrespective of the permeability conditions. This might be due the flexibility of the flag in which the flag can change its shape in response to the low fluid pressure acting on the surface. A pair of longitudinal vortices rotating in opposite directions is generated at both spanwise ends of the flapping flag. Their strengths vary in accordance with the instantaneous lift force. When the flag is impermeable, these longitudinal vortices are connected to the spanwise vortex shed from the trailing edge and deform into a V-shaped vortex downstream. Conversely, the longitudinal vortices generated from a permeable flag simply move downstream without reconnecting. In addition, it is found that fluid permeation takes place at the location where the work by the fluid on the flag is concentrated.

Keywords: flag, permeability, fluid-structure interactions, incompressible SPH.

1. Introduction

The flapping of a flag is a self-excited vibration that occurs when a thin flexible sheet separates two flows. This type of vibration accompanying oscillation and the deformation of structures is a so-called flow-induced vibration (Paidoussis 2014). In general, fluid machineries are designed to avoid these flow-induced vibrations because they are sometimes strong enough to destroy the structures themselves. However, if one can make use of this powerful energy, it may become a new energy source. Recently, various devices have been proposed to convert flow-induced vibrations into electricity. Such attempts are called fluid-energy harvesting. For example, Michelin & Doaré (2013) attempted to generate electricity by attaching a piezo element to a plastic flag where the strain energy generated by the deformation of the flag was converted into electricity. Bae et al. (2014) devised a power generator making use of the static electricity generated when a metal-coated cloth flapped and grazed against a copper plate. Zhao et al. (2016) manufactured a system using a flag made by weaving fibers coated with several types of metals. The flag was launched to high altitudes using a balloon. Even though these generators are compact and are not aimed at replacing conventional wind turbines, they are generating a considerable amount of attention due to their high efficiencies in power generation. It is important to understand the fundamental characteristics and the oscillating mechanisms of a flag in a uniform flow in order to actively use these oscillations for fluid-energy harvesting.

The flapping motion of a flag of streamwise length L and mass-per-length $\rho_s h_s$ in a fluid flow of density ρ, viscosity μ, and uniform velocity U_∞ can be characterized by several non-dimensional parameters. When the motion is two dimensional, i.e., the spanwise variation is negligible, the flag motion is associated with the bending rigidity and the structure-to-fluid mass ratio (the areal density ratio), in addition to the Reynolds number (Connell & Yue 2007, Alben & Shelley 2008), which are given by

$$Re = \frac{\rho U_\infty L}{\mu}, \quad B^* = \frac{D}{\rho U_\infty^2 L^3}, \quad M^* = \frac{\rho_s h_s}{\rho L}, \tag{1}$$

where D is the bending stiffness per unit defined by

$$D = \frac{E h_s^3}{12(1-\sigma^2)}. \tag{2}$$

In these equations, E is Young's modulus and σ is Poisson's ratio. The bending rigidity B^* and the areal density ratio M^* differ depending on the flag material. In other words, the power generation efficiency using flags can be improved by an appropriate selection of the material and weaving method.

The vibration modes of flapping flags were first studied by Taneda (1968) for four different materials: silk, muslin, flannel, and canvas. He reported that the flags remained stationary without flapping when the flow velocity was approximately $1-2$ m/s, whereas various periodic vibration modes could be observed at higher flow velocities. Zhang et al. (2000) conducted experiments of a flapping filament in a soap film, which modeled a one-dimensional flag placed in a two-dimensional flow, and found that the flag had two stable

states depending on its length. One was a static stable state (stretched-straight state) in which the flag did not flap, and the other was a dynamic stable state (flapping state) in which the flag flapped periodically. They also reported that there was a hysteresis in the relationship between the filament length and the switching of the stable/unstable states. This discovery attracted attention because it contradicted the well-accepted idea (Rayleigh 1878) that flags were always in the flapping state due to the Kelvin-Helmholtz instability. Later, studies on the critical velocity that marked the beginning of the flapping state were performed. Eloy et al. (2008) investigated the influence of the flag's aspect ratio on the critical velocity. Argentina & Mahadevan (2005) performed an analysis of the critical velocity using a mathematical analysis model.

Studies using numerical simulations have also been performed. The constitutive equations of a sufficiently thin body and the Navier-Stokes equations of an incompressible viscous flow have been coupled in several ways, for example by the arbitrary Lagrangian-Eulerian (ALE) finite element method (Sawada & Hisada 2007), the fluid-structure direct simulation (FSDS) (Connell & Yue 2007), or the immersed boundary (IB) method (Huang & Sung 2010, Zhu et al. 2014). In addition to these grid-based Eulerian methods, grid-free Lagrangian methods in which the wake is represented by vortex sheet elements (Alben & Shelley 2008) or discrete point vortices (Michelin et al. 2008) have been performed. Choi & Ko (2002) proposed another particle-based model in which a structure is represented by a group of particles connected to each other via a spring from the viewpoint of computer graphics applications. Harada et al. (2007) incorporated a cloth model based on a linear spring into the smoothed particle hydrodynamics (SPH) method to simulate the interaction between fluids and cloth in real time using graphics processing units (GPUs). Lagrangian methods have advantages in terms of the computational time and the ease of implementation compared to grid-based Eulerian methods because the deformation of an object is automatically represented by an element's movements.

It is common knowledge through experience that the fluttering motion of actual flags depends on their materials. For example, loosely woven fabric called bunting Wilson (1999) has been widely used as national flags or signal flags since the beginning of the history of flags. Appropriate gaps between the fibers make a flag more airy and moderately breathable which help the flag to flutter more beautifully in the wind. And these materials also hold colors over a long period of time. In recent years, the flag fabric being highly breathable, elastic and extremely durable was developed for outdoor advertising banners. The permeability of such flags or banners reaches approximately 50%. Choosing the right material can also suppress the noise generation in the strong wind. However, how the permeability affect the flag behavior is not well known because the flags were treated as impermeable in most the past analyses. In addition, when a flag is used for power generation, there is a possibility of improving its efficiency through appropriately choosing the material and the method of weaving.

In the present study, three-dimensional numerical simulations are performed using an incompressible SPH method, which has already been presented in our previous work,

e.g., (Ito et al. 2015). The effect of permeability on the dynamics of flags in a uniform flow is examined under various Reynolds numbers. The permeable flag is modeled by changing the configuration of dummy particles. Wind tunnel experiments are also performed to check the validity of the newly proposed permeable model.

2. Incompressible SPH method

2.1. Fluid simulation

An incompressible flow field is simulated using a density homogenization algorithm (Ito et al. 2015) based on a predictor-modifier method in which the particle velocities are corrected to smooth the local density deviation instead of solving the Poisson pressure equation. An outline of the method is shown in Fig. 1. First, the velocity of particle a obtained at the previous time step is chosen as the initial value of the velocity predictor at the present time step (Fig. 1(a)). Accordingly, particle a moves with the velocity predictor

$$\boldsymbol{v}_{a,\mathrm{pred}}^{(0)}(t) = \boldsymbol{v}(t - \Delta t). \tag{3}$$

Because this predictor is estimated irrespective of the motions of the other particles, the density distribution given by the particle arrangement becomes uneven after all particles tentatively move. Therefore, as shown in Fig. 1(b), a velocity corrector $\boldsymbol{v}_{a,\mathrm{corr}}$ is calculated to smooth the local density gradient:

$$\boldsymbol{v}_{a,\mathrm{corr}}^{(k)} = -C \sum_b \left(\frac{\tilde{\rho}_a^{(k)} - \rho_0}{\tilde{\rho}_a^{(k)2}} + \frac{\tilde{\rho}_b^{(k)} - \rho_0}{\tilde{\rho}_b^{(k)2}} \right) \nabla_a W_{ab}, \tag{4}$$

where C is a constant that determines the amount of correction, ρ_0 is the reference density of the fluid, and $\tilde{\rho}^{(k)}$ is the density at the tentative particle location. The notation $\nabla_a W_{ab}$ indicates the gradient of a symmetric kernel function taken with respect to the coordinates of the particle a. We use a cubic spline kernel instead of a Gaussian kernel to reduce the computational cost, which is

$$W_{ab} = \frac{1}{\pi h^3} \begin{cases} 1 - \dfrac{3}{2}q^2 + \dfrac{3}{4}q^3 & (0 \le q < 1) \\ \dfrac{1}{4}(2 - q^2) & (1 \le q < 2) \\ 0 & (2 \le q) \end{cases} \tag{5}$$

where $q = |\boldsymbol{r}_{ab}|/h$ and h is the smoothing length. The velocity predictor is then updated by adding the modifier $\boldsymbol{v}_{a,\mathrm{corr}}^{(k)}$, and all the particles are moved again in accordance with the new predictors. By repeating this process N times, the density at each particle $\tilde{\rho}$ gradually approaches ρ_0 and the density inhomogeneity is reduced. After N operations, the adjusted velocity is

$$\boldsymbol{v}_{a,\mathrm{adj}} = \boldsymbol{v}(t - \Delta t) + \sum_{k=1}^{N} \boldsymbol{v}_{a,\mathrm{corr}}^{(k)}, \tag{6}$$

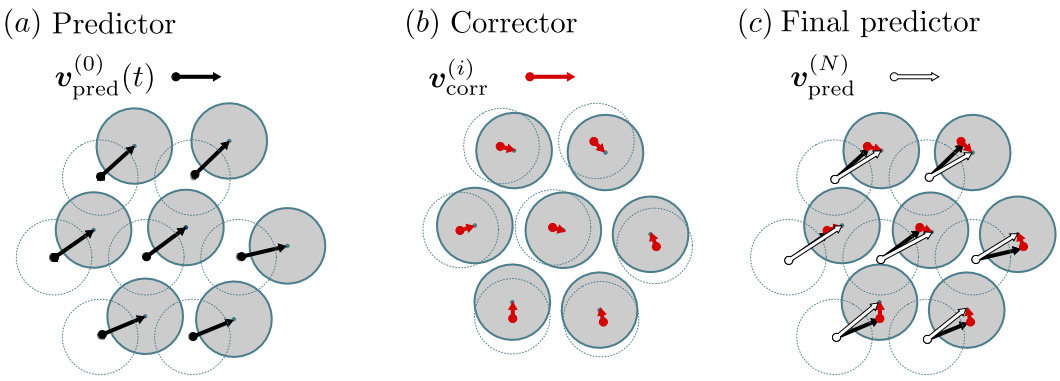

Figure 1. Adjustment of particle velocities via the predictor-corrector method.

as shown in Fig. 1(c). The number of iterations N is set to 5 because larger N will increase the numerical viscosity. The velocity at the next step $\boldsymbol{v}_a(t + \Delta t)$ is finally obtained by taking into account the viscosity effect and the external forces. The density gradient in Eq. (4) produces a symmetric central force between pairs of particles a and b such that the linear and angular momenta are conserved during the density homogenizing process.

2.2. Fluid-structure interaction

A flag is represented by a single layer of particles arranged in a sheet shape with constraints between the particles. Figure 2 shows the modeling of the forces acting on the flag, where the elastic force and the bending rigidity are modeled on the basis of the spring-mass model (Harada et al. 2007) and the particle-based model (Yamada & Suzuki 2005), respectively. Two types of springs are used between the neighboring particles to model the former elastic force, as shown in Figs. 2(a) and 2(b). The force $\boldsymbol{T}_i$ between two adjacent particles (i, j) represents the stretching force, while the force $\boldsymbol{S}_i$ between the two particles (i, k) on a diagonal line represents the shearing force. Assuming that they are proportional to the change in the distance between the particles, we obtain the following equations via Hooke's law:

$$\boldsymbol{T}_i = \sum_i k_T \left(|\boldsymbol{x}_{ij}| - l_T\right) \frac{\boldsymbol{x}_{ij}}{|\boldsymbol{x}_{ij}|}, \qquad \boldsymbol{S}_i = \sum_k k_S \left(|\boldsymbol{x}_{ik}| - l_S\right) \frac{\boldsymbol{x}_{ik}}{|\boldsymbol{x}_{ik}|}, \tag{7}$$

where $\boldsymbol{x}_{ij}$ is the displacement vector between the ith and jth flag particles and l_T and l_S are the natural lengths of the spring related to the stretching and shearing motions with spring constants of k_T and k_S, respectively. When these spring constants become larger, the flag approaches the inextensible condition. In this study, k_T and k_S are set to 5.0×10^4 in reference to Young's modulus of the cloth used in the experiments. The latter bending moment is also modeled using a flat spring connecting the neighboring particles (i, l) or (i, m), as shown in Fig. 2(c). The magnitude of the bending moment M_i acting on the particle i is given by

$$M_i = \sum_{l,m} D\kappa_i, \tag{8}$$

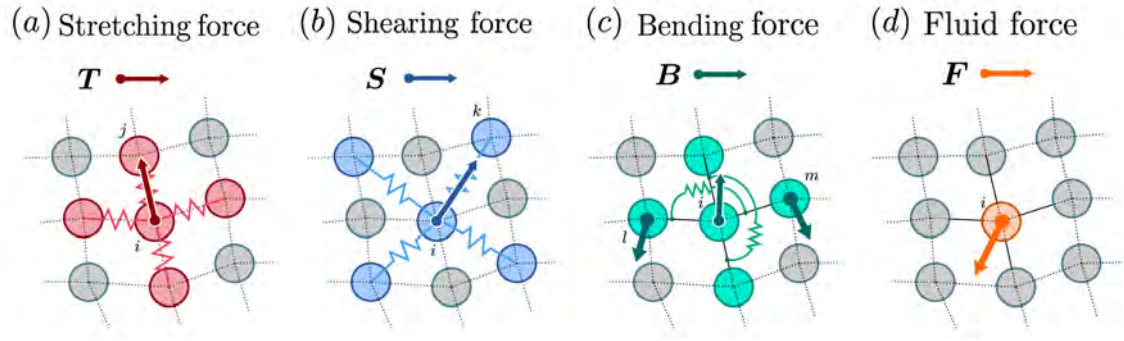

Figure 2. Modeling of the forces acting on a flag.

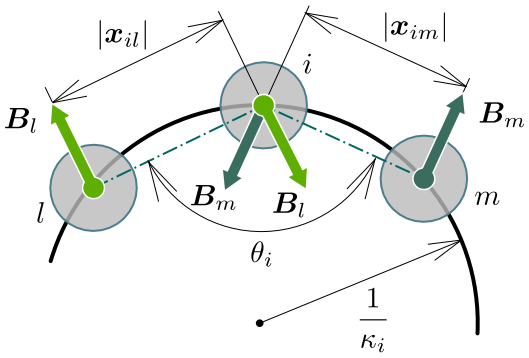

Figure 3. Calculation of the curvature.

where κ_i is the curvature at the location of particle i. The curvature κ_i is obtained from the sine theorem and the cosine theorem as the reciprocal of the radius of a perfect circle passing through three points (l, i, m), as shown in Fig. 3,

$$\kappa_i = \frac{2\sqrt{1-\cos^2\theta_i}}{\sqrt{|\boldsymbol{x}_{il}|^2 + |\boldsymbol{x}_{im}|^2 - 2|\boldsymbol{x}_{il}||\boldsymbol{x}_{im}|\cos\theta_i}}. \tag{9}$$

The forces $\boldsymbol{B}_l$ and $\boldsymbol{B}_m$ derived from the bending moments acting on the particles l and m can be written as

$$\boldsymbol{B}_l = \frac{M_i}{|\boldsymbol{x}_{il}|}\boldsymbol{n}_l, \quad \boldsymbol{B}_m = \frac{M_i}{|\boldsymbol{x}_{im}|}\boldsymbol{n}_m, \tag{10}$$

where $\boldsymbol{n}_l$ and $\boldsymbol{n}_m$ are the unit normal vectors at the locations of particles l and m, respectively. The direction in which the bending is relaxed is defined as positive. The resulting force of $\boldsymbol{B}_l$ and $\boldsymbol{B}_m$ for particle i is then given by

$$\boldsymbol{B}_i = -\frac{M_i}{|\boldsymbol{x}_{il}|}\boldsymbol{n}_l - \frac{M_i}{|\boldsymbol{x}_{im}|}\boldsymbol{n}_m. \tag{11}$$

Special treatment is required to evaluate the force that the flag receives from the fluid because the pressure does not explicitly appear in the present incompressible SPH method. The amount of velocity correction during the density homogenizing process is

$$\boldsymbol{v}_{i,\mathrm{final}} - \boldsymbol{v}^{(0)}_{i,\mathrm{pred}} = \left[-\frac{1}{\rho_i}(\nabla p)_i\right]\Delta t. \tag{12}$$

Assuming that the adjustments of the particle velocities are due to the local pressure gradients, we have

$$(\nabla p)_a = -\frac{\rho_a}{\Delta t}(\boldsymbol{v}_{a,\mathrm{final}} - \boldsymbol{v}^{(0)}_{a,\mathrm{pred}}). \tag{13}$$

Note that this treatment is limited to the fluid particles because the flag particles do not move during the density homogenizing process. Instead, the force acting on each flag particle $\boldsymbol{F}_i$ can be estimated by integrating the reaction forces from the fluid particles located next to the flag particle. The effects from the fluid particles on both the front and reverse sides of the flag are taken into account. Even though the direction of $\boldsymbol{F}_i$ is not necessarily exactly normal to the local flag surface due to the discrete particle distribution, it is confirmed that the actual directions are fairly close to normal.

From the above discussion, the equations of motion of the flag are given by

$$\rho_s h S \frac{\mathrm{d}^2 \boldsymbol{r}_i}{\mathrm{d}t^2} = \boldsymbol{T}_i + \boldsymbol{S}_i + \boldsymbol{B}_i + \boldsymbol{F}_i. \tag{14}$$

The velocity and position at the next time step are obtained by numerically integrating Eq. (14) with respect to time. The time step of the fluid calculation Δt needs to satisfy the Courant-Friedrichs-Lewy (CFL) condition,

$$\Delta t \leq \alpha \frac{h}{U_{\max}}, \tag{15}$$

where $U_{\max}$ is the maximum velocity and α is a constant of approximately 0.1 – 0.3. In this study, we chose $\alpha = 0.1$ and Δt =1.0 $\times$ 10^{-4}. Compared to the conventional compressible SPH method, Δt can be much larger in incompressible SPH; however, a large time increment will make the structure computation unstable (Tada et al. 2011). Therefore, the time step of the structure computation was empirically determined to be $\Delta t_s = \Delta t/200$.

3. Problem setting

3.1. Experimental setup

A schematic view of the experimental setup is shown in Fig. 4. The flag is a square-shaped cloth, 40 mm on a side, horizontally mounted in a uniform flow at the outlet of a nozzle. The nozzle size of the blower-type wind tunnel is 265 mm $\times$ 500 mm. The upstream edge of the cloth is pinched between two plates each 0.5-mm thick and 10-mm long streamwise. The origin of the coordinate system is placed at the center of the leading edge of the cloth, where the x, y, and z axes denote the streamwise, vertical, and spanwise directions, respectively. The flapping amplitude is defined as the maximum vertical displacement of the trailing edge of the cloth. Images of the cloth motion were taken using a high-speed camera (Nikon 1, 1200 fps, 400×144 pixel).

Two types of cloths were prepared to be used as impermeable and permeable flags. A permeable flag was made by punching 14 $\times$ 14 holes with diameters of 1.5 mm at an

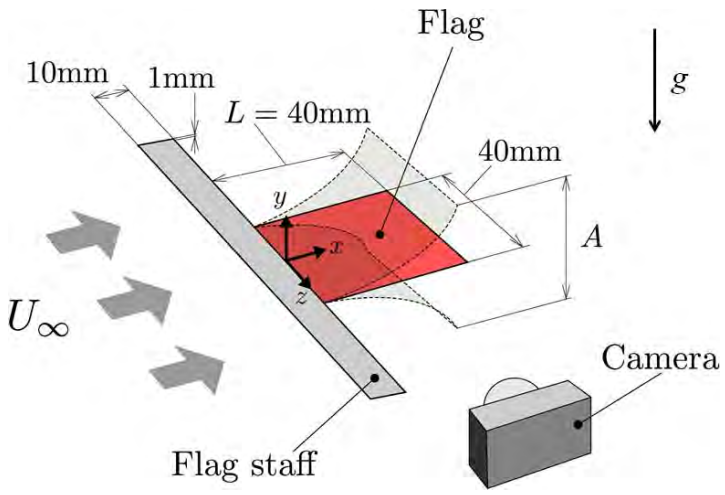

Figure 4. Schematic view of the experimental setup.

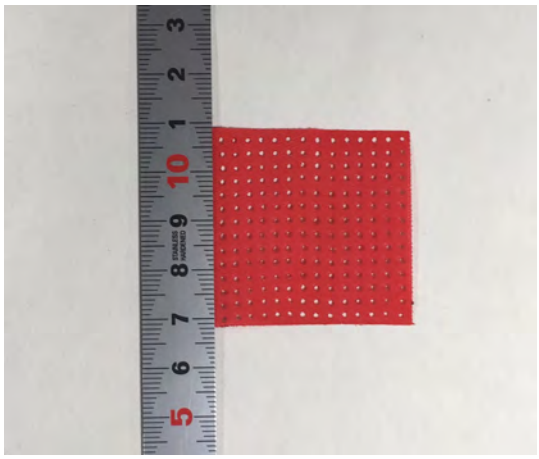

Figure 5. Material used in the permeable flag experiments.

interval of 2 mm into the cloth, as shown in Fig. 5. Here the permeability ϕ is defined as the porosity given by

$$\phi = \frac{S_p}{S_0}, \tag{16}$$

where S_0 is the area of the smoothed cloth without holes, i.e., L^2, and S_p is the sum of the cross-sectional areas of the holes. The permeability of the punched flag is then $\phi = 0.22$.

When there is no wind, the tail of the cloth droops down due to its own weight. The flexural rigidity of the cloth can be estimated by measuring its deflection curve. The values of the physical properties of the flag are summarized in Table 1. The range of the uniform velocity at the outlet of the wind tunnel is changed from 6 m/s to 10 m/s. Therefore, the Reynolds number is in the range of $Re = 1.6$ – $2.7\times\ 10^4$. In addition, the bending stiffness is in the range of $B^* = 1.6$ – $3.2\ \times\ 10^{-3}$. The areal density ratio is kept constant at $M^* \simeq 2.4$.

Table 1. Physical properties of the flag..

Material	Polyester
Length of one side, L	4.0×10^{-2} m
Width, b	4.0×10^{-2} m
Thickness, h_s	1.1×10^{-4} m
Density, ρ_s	1.1×10^{3} kg/m^3
Bending stiffness per unit width, D	1.2×10^{-5} N $\cdot$ m
Permeability, ϕ	0, 0.22

3.2. Numerical conditions

The numerical simulations were performed under the same conditions as the experiments. The computational domain is shown in Fig. 6. In addition to the field coordinate system of (x, y, z), which is the same as the experiments, we define one more coordinate system of (ξ, ζ) to specify the position on the curved surface of the flapping flag. A flag whose side length is L is horizontally placed in the mid-plane of the domain, a distance L from the inlet boundary, at the initial state. Two computational domains are prepared to check the domain dependence of the flag motion: $6.4L \times 4L \times 2.5L$ and $3.2L \times 2L \times 2L$. The large region consists of $260 \times 160 \times 100$ particles, and the small region consists of $130 \times 80 \times 80$ particles. A uniform flow of velocity U_∞ is given at the inflow boundary, and the Neumann condition is given at the outflow boundary. Periodic boundary conditions are used in both the y and z directions.

The flag consists of 41×41 particles in the xz plane and one particle in the y direction. The permeability of the flag is modeled by removing some particles allowing the fluid particles to penetrate the flag. Figure 7 shows the particle distribution for three different permeability conditions: impermeability ($\phi = 0$), low permeability ($\phi = 0.24$), and high permeability ($\phi = 0.5$). The low-permeability condition is close to that of the $\phi = 0.22$ experiment. The behavior of the flag is computed at the red-colored points in the figure. These flag particles are placed $2h$ apart, and there are 21×21 points in total. This method was chosen so that the permeability of the flag can be changed without changing the structural characteristics of the flag. Dummy particles, which block the fluid particles from penetrating the flag, are placed in-between the flag particles. Accordingly, changing the number of dummy particles changes the permeability of the flag. The impermeable case (Fig. 7(a)), low-permeability case (Fig. 7(b)), and high-permeability case (Fig. 7 (c)) are compared.

The areal density ratio is fixed to $M^* = 2.4$, which is the same as the experiments. The Reynolds number Re and the bending stiffness B^* are changed depending on the uniform velocity U_∞ so that both non-dimensional numbers match those of the experiments. In the following, the spatial coordinates x, y, and z and time t are non-dimensionalized using the uniform flow velocity U_∞ and the flag length L. The symbol * indicates a non-dimensional variable.

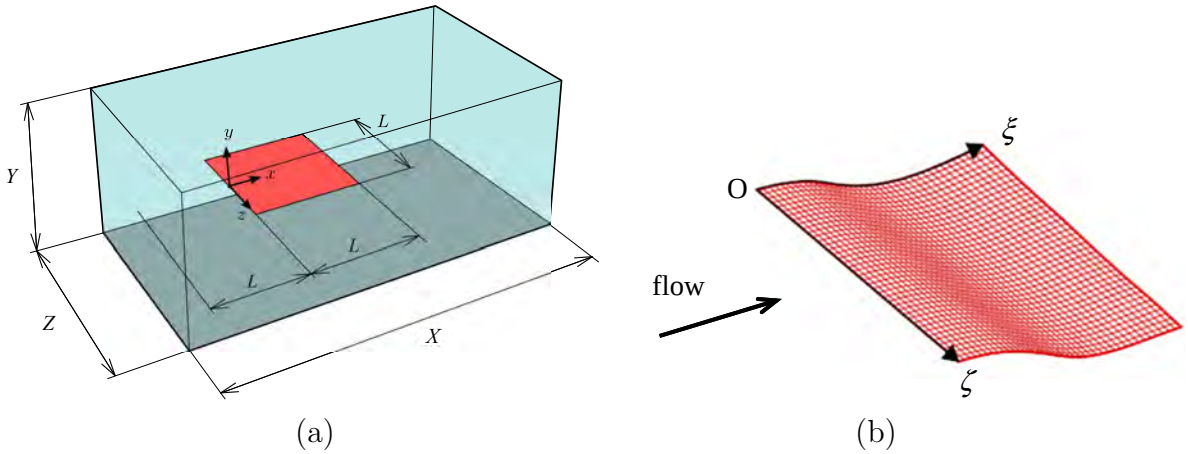

(a) (b)

Figure 6. Sketches of (a) the numerical setup and (b) the flag coordinate system.

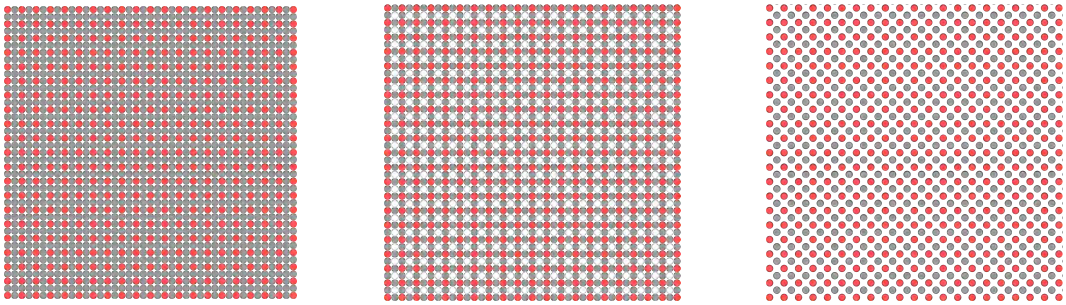

(a) $\phi = 0$ (b) $\phi = 0.24$ (c) $\phi = 0.5$

Figure 7. Particle distribution of flags with different permeabilities. Red particles indicate flag particles, and gray particles indicate dummy particles.

4. Results and discussion

4.1. Vibration modes in the experimental observations

First, the vibration modes of the impermeable and permeable flags in the experiments were examined while changing the freestream velocity. Figure 8 shows the variation in the non-dimensional amplitude $A^* = A/L$ and the flapping frequency $f^* = fL/U$ for different Reynolds numbers Re.

Hysteresis can be observed in the behaviors of both flags. When the Reynolds number is low, the impermeable flag remains stationary in the straight position (stretched-straight state). The flag starts to oscillate periodically when the Reynolds number exceeds $Re = 2.1 \times 10^4$ (flapping state). The flapping is two-dimensional in the spanwise direction. As the flow velocity further increases, the amplitude and frequency of the vibration monotonically increases. However, the flag remains in the flapping state until $Re = 1.9 \times 10^4$ when the flow velocity is reduced. The impermeable flag becomes bistable in the range of $Re = 1.9 - 2.1 \times 10^4$. In the bistable state, the flag is sensitive to external stimuli. By lightly touching the flag with a stick, the vibration mode can be switched from the stretched-straight state to the flapping state and vice-versa. Similar

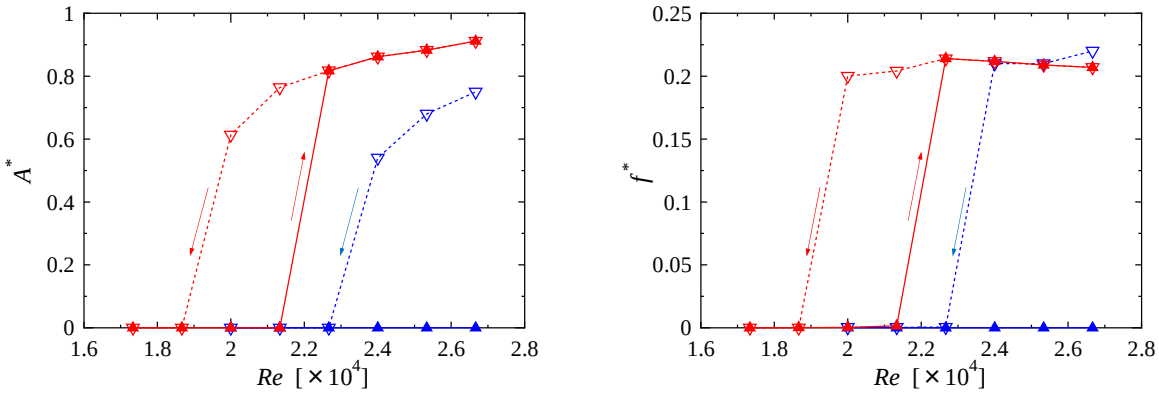

Figure 8. Reynolds number Re versus (left) the non-dimensional amplitude A^*, and (right) the non-dimensional frequency f^*. The red line indicates the impermeable flag ($\phi = 0$), and the blue line indicates the permeable flag ($\phi = 0.22$).

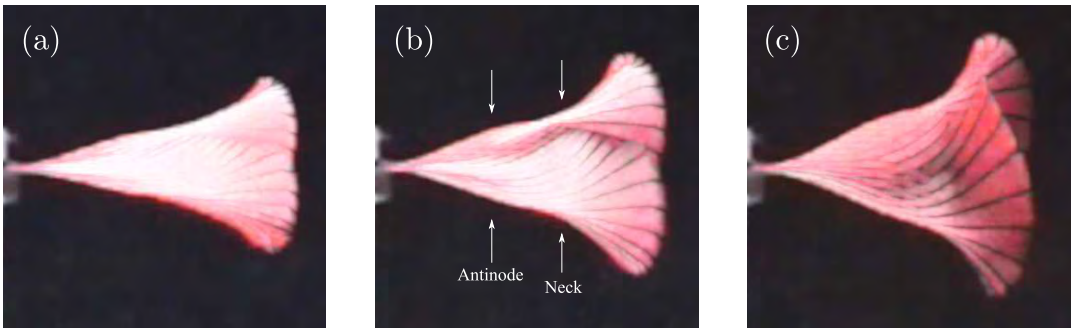

Figure 9. Superimposed images of the oscillating impermeable flag for Re numbers of (a) 2.0×10^4, (b) 2.1×10^4, and (c) 2.7×10^4.

hysteresis phenomena have also been reported in other experiments, including the one-dimensional flag in the soap film flow (Eloy et al. 2008, Shelley & Zhang 2011).

As for the permeable flag in the experiments, the spontaneous start of oscillations could not be observed under the Reynolds number conditions of our test. However, when the Reynolds number exceeded $Re = 2.4 \times 10^4$, the flag could easily be shifted to the flapping state or back to the stretched-straight state by touching the flag slightly with a stick. When the Reynolds number falls below $Re = 2.4 \times 10^4$, the flag stays straight regardless of the external stimuli. Compared to the impermeable flag, the amplitudes of the oscillations of the permeable flag are smaller in all velocity ranges, even though the frequency is the same regardless of the permeability.

Figure 9 shows multiple exposed images of the impermeable flag in the flapping state at $Re = 2.0 \times 10^4$, 2.1×10^4, and 2.7×10^4. Each image is created as a superimposition of consecutive images during one flapping period. The trajectory of the trailing edge of the flag draws a "doglegged shape". In addition, one antinode and one neck can be observed in the oscillation. These oscillating characteristics and the velocity range where the bistable state appears agree well with the prediction by Eloy et al. (2008) using linear stability theory.

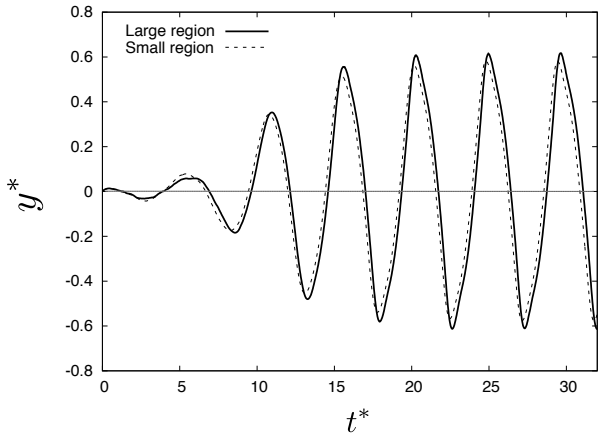

Figure 10. Effect of the computational domain size. Impermeable flag case when $Re = 2.2 \times 10^4$.

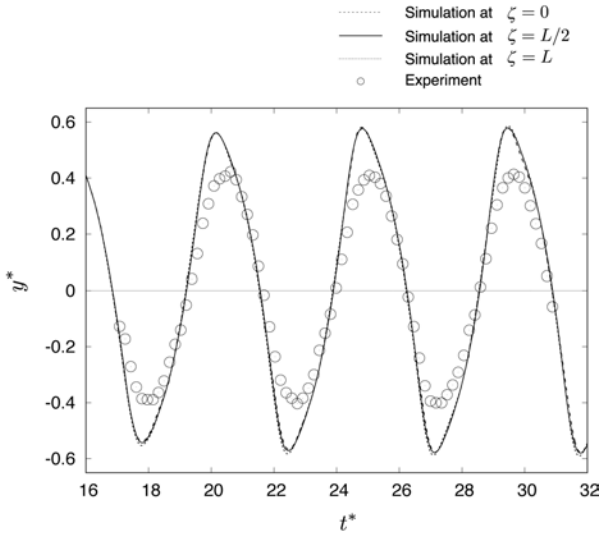

Figure 11. Temporal displacement of the three free-end points at $(\xi, \zeta) = (L, 0)$, $(L, L/2)$, and (L, L) for $Re = 2.2 \times 10^4$ and $B^* = 2.2 \times 10^{-3}$.

4.2. Validation of coupled code

The motion of an impermeable flag was simulated using large and small computational domains to check whether the domain was sufficiently large. Figure 10 compares the time variations of the vertical displacements of the trailing edges, $\xi = L$, of the two domains. Both profiles agree well with each other. Because the size of the computational domain has little effect to the movement of the flag, we decided that the smaller domain was sufficient for this computation.

The results of the smaller domain computation were also compared to the experimental data and are shown in Fig. 11. The data are of three oscillation periods at $Re = 2.2 \times 10^4$ ($U_\infty = 8.5$ m/s) after $t^* = 16$, when the oscillation became periodic. Even though the amplitude of the flag is 20% larger than that of the experiments,

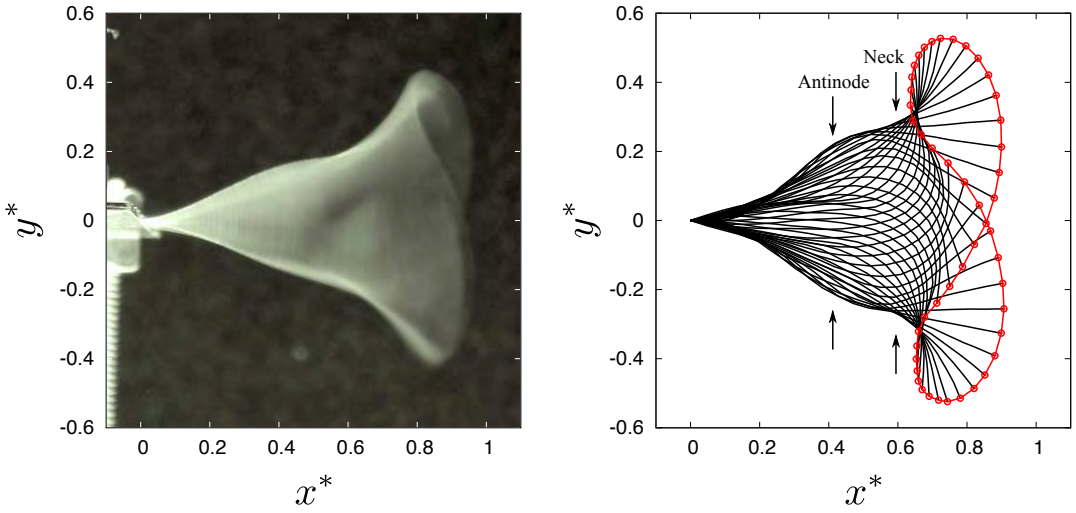

Figure 12. Comparison of the flag trajectories for an impermeable flag at $Re = 2.2 \times 10^4$ and $B^* = 2.2 \times 10^{-3}$: (left) experimental result recorded via long-exposure photography and (right) the simulation ($\zeta = L/2$).

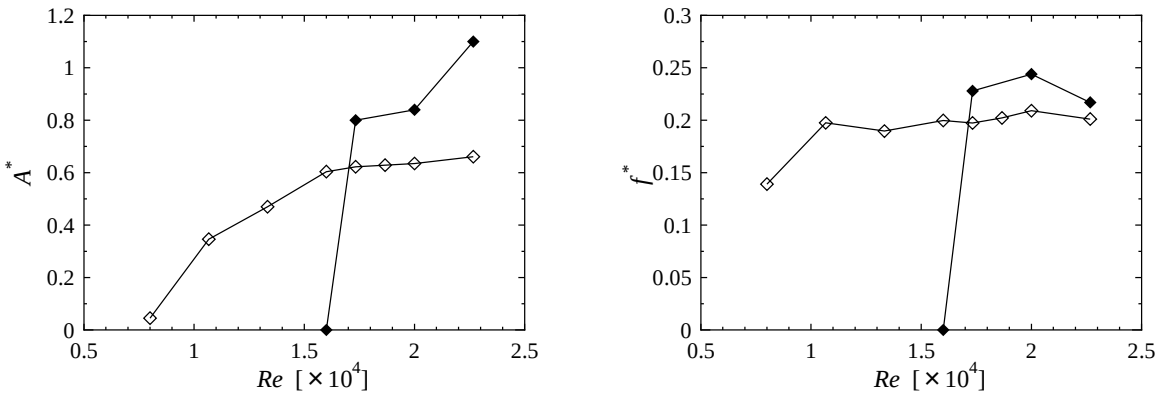

Figure 13. Reynolds number Re versus (left) the non-dimensional amplitude A^*, and (right) the non-dimensional frequency f^*. The closed diamond indicates the impermeable flag ($\phi = 0$), and the open diamond indicates the permeable flag ($\phi = 0.24$).

the oscillation period is nearly identical. In addition, the envelope shape showing the oscillating motion through one cycle is also in good agreement with the experiments, as shown in Fig. 12. However, note that the hysteresis in the mode change caused by the change in the uniform velocity is not observed in the simulation (see, Fig. 13). Although the computation was carried out for a considerably long period, mode change could not be observed.

4.3. Flapping motion in permeable conditions

Numerical simulations of the permeable flags were also conducted and compared to the impermeable flag case. The variation in the non-dimensional amplitude A^* and the flapping frequency f^* for different Reynolds number Re is shown in Fig. 13. When

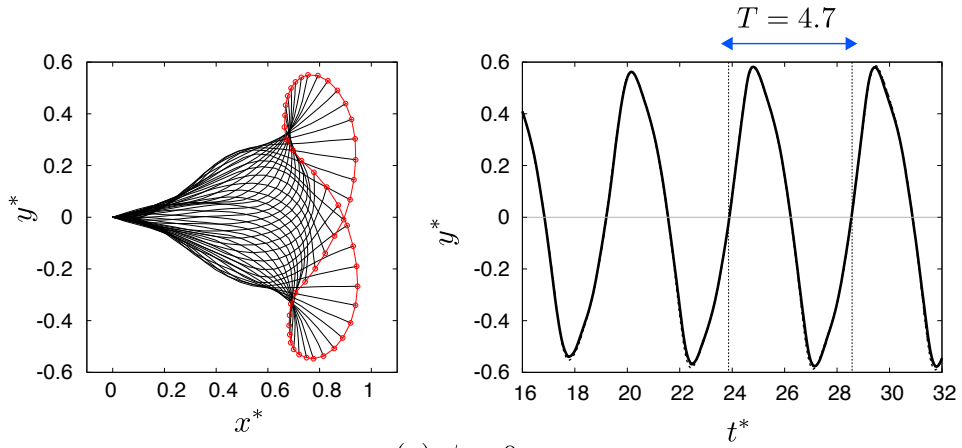

(a) $\phi = 0$

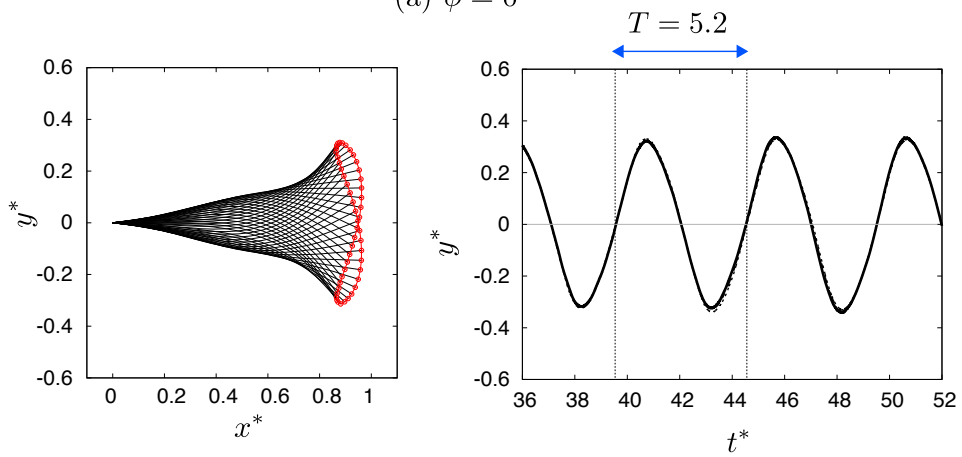

(b) $\phi = 0.24$

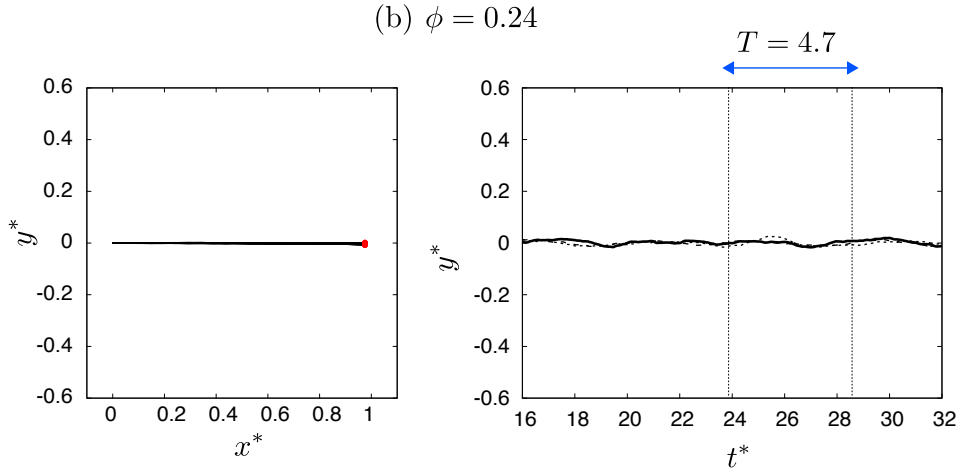

(c) $\phi = 0.5$

Figure 14. Comparison of the flag locations and vertical displacements of the three free-end locations ($\xi = L$) with various permeabilities at $\zeta = 0$. - - -, $\zeta = L/2$; · · · · ·, $\zeta = L$; ——. In all cases, $Re = 2.2 \times 10^4$ and $B^* = 2.2 \times 10^{-3}$.

the flag is permeable, both the amplitude and the frequency of fluttering motion are slightly lower than those of the impermeable flag. Interestingly, although its amplitude is very small, the flag keeps oscillating even in the small Reynolds number region. The stretched-straight state which was present in the experiment, as shown in Fig. 8, cannot

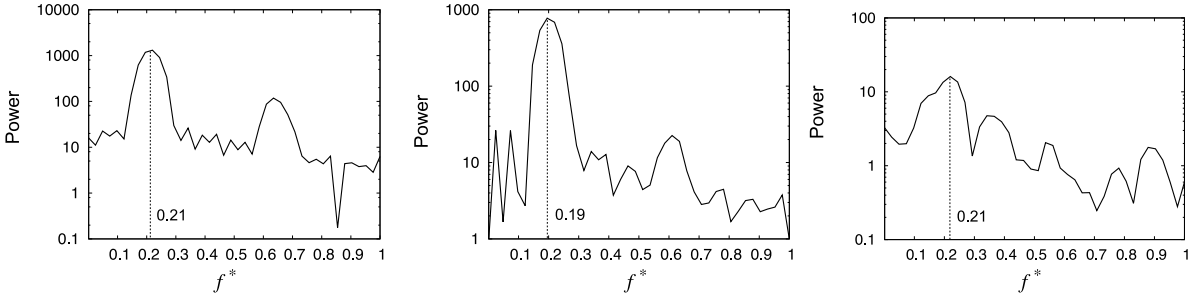

(a) $\phi = 0$ (b) $\phi = 0.24$ (c) $\phi = 0.5$

Figure 15. FFT analyses of the movement of the trailing edge $(\xi, \zeta) = (L, L/2)$ with changing permeability ϕ when $Re = 2.2 \times 10^4$ and $B^* = 2.2 \times 10^{-3}$.

be observed in the simulation. This discrepancy might be due to the deterioration in rigidity caused by regularly punched holes in Polyester cloth of the flag, which is ignored in simulation. Anyway, the present result suggests that the permeable flags have potential to improve the energy harvesting performance.

Figure 14 shows the oscillatory behavior of the permeable flag at $Re = 2.2 \times 10^4$ and how the free end of the flag moves. When the permeability ϕ of the flag is 0.24, the flag oscillates two dimensionally in the single-neck mode. The trajectory of the central free end, $\zeta = L/2$, draws a "doglegged shape", similar to the case of the impermeable flag. The amplitude is reduced to approximately 0.3, which is approximately 50% smaller than that amplitude at the impermeable condition of $\phi = 0$. For the higher permeability condition of $\phi = 0.5$, the flag remains stationary without oscillating. The oscillating frequency of the $\zeta = L/2$ point was analyzed via fast Fourier transform (FFT). The results are shown in Fig. 15. In this figure, the horizontal axis is the non-dimensional frequency $f^* = fL/U_\infty$, which corresponds to the Strouhal number. A strong peak appears at $f^* = 0.21$ ($f = 45$ Hz) in the impermeable condition, reflecting the periodic oscillation of the flag. When the flag has a low permeability of $\phi = 0.24$, the dominant peak shifts slightly to the lower side, $f^* = 0.19$ ($f = 40$ Hz). When the permeability is increased to $\phi = 0.5$, the peak level falls to nearly 1/100 of the impermeable flag case because the flag stays in the stretched-straight state. A flag with a permeability of $\phi = 0.5$ will not oscillate even when a velocity of $0.2U_\infty$ in the vertical direction is given to the trailing edge as an initial condition.

Trajectories of the free ends, $(\xi, \zeta) = (L, 0)$, $(L, L/2)$ and (L, L), are drawn in the phase diagrams. The horizontal and vertical axes in Fig. 16 represent the displacement y^* and the velocity v^* in the vertical direction, respectively. Each red circle with letters "a" to "f" in the figure represents the time which will be shown later in Fig. 25. Experimental results are also plotted in Fig. 17 for comparison. Here, the flag tail positions were obtained from a successive frame-by-frame still image of a movie of five flapping cycles. For all cases, the free ends of the flag draw nearly rectangular orbits in the counter clockwise direction, though some differences are found in the spanwise direction. These orbits are inclined with the longer axis in the first and third quadrant

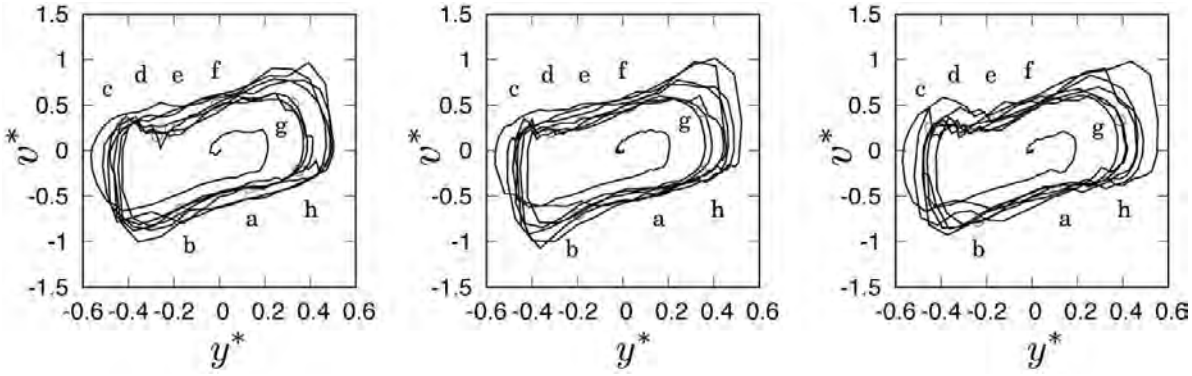

(a) $\phi = 0$

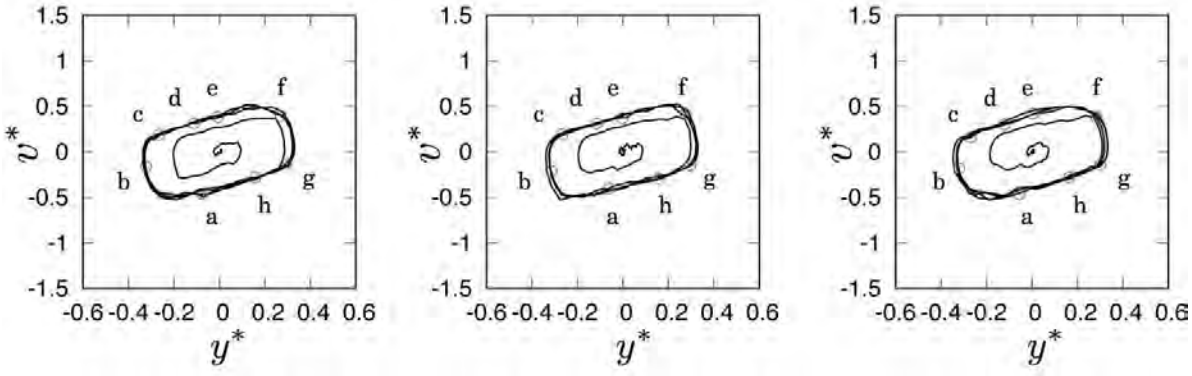

(b) $\phi = 0.24$

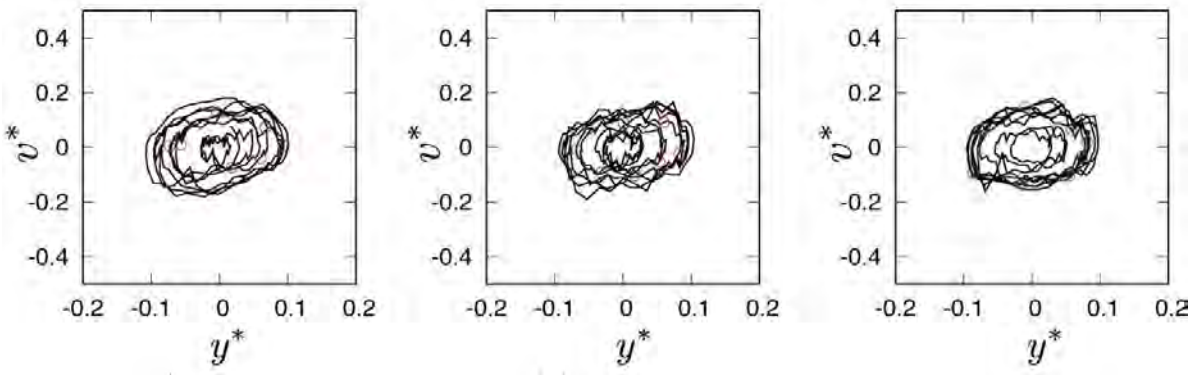

(c) $\phi = 0.5$

Figure 16. Phase diagram of free ends at $(\xi, \zeta) = (L, 0)$ (left), $(l, L/2)$ (center) and (L, L) (right) in y^* v^* plane with various permeabilities at $Re = 2.2 \times 10^4$ and $B^* = 2.2 \times 10^{-3}$.

directions, which reflect the "doglegged shape" trajectory shown in Fig. 14. However, in the experiment, the trajectories are close to an ellipsoid and their inclined angles are smaller than those in the simulation. This discrepancy may be driving from the flagstaff which is present only in the experiment. The size of the rectangular orbit becomes small when the permeability is high. Interestingly, the two dimensionality of the flapping motion is enhanced when the flag has some permeability (Fig. 16 (b)). Also, even when the permeability of the flag is high at $\phi = 0.5$, the orbit shape still remains

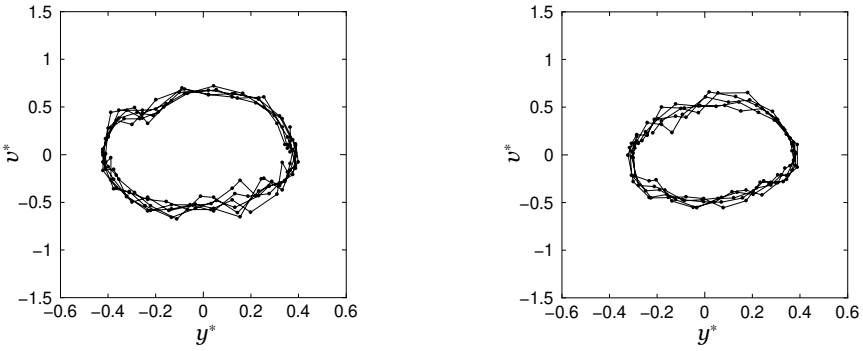

(a) $\phi = 0$ (b) $\phi = 0.22$

Figure 17. y^* v^* phase diagram of experimental data at $Re = 2.2 \times 10^4$.

rectangular, even though the trajectory is smaller and is highly disturbed compared to other two cases.

Figure 18 shows the time variations of the flapping motions for the three flags with different permeabilities. The oscillation period T^* is obtained from the frequency at the maximum peak in each spectrum shown in Fig. 15. The elapsed time from the moment the free end of the flag crosses the horizontal plane at $y^* = 0$ in the positive direction is denoted by t', and four sequential pictures of each flag are shown. The flag particles are colored black. The fluid particles that have passed from the reverse side (lower side) to the front side (upper side) of the flag are colored red, and those that passed in the opposite direction are colored blue. For the low-permeability condition of $\phi = 0.24$, a flow through the flag from the front side to the reverse side of the flag is generated when the flag moves up, while a flow from the reverse side to the front side is generated when the flag moves down. Therefore, a group of red particles is released from the upper surface into the wake through the first half of the period and then a group of blue particles is released from the lower surface through the latter half of the period. Conversely, for the high-permeability condition of $\phi = 0.5$, because the flag does not oscillate, the permeated particles move downstream in two layers and there are no differences between the phases.

Figure 19 shows the probability distribution of the numbers of permeating particles in the (ξ, ζ) plane, where the red region indicates the region in which many fluid particles permeate, while the blue region is the region in which permeations rarely take place. For the permeability condition of $\phi = 0.24$, 19,283 particles pass through the flag during one oscillation cycle. In detail, 9,571 particles move from the upper surface to the lower surface (the red particles in Fig. 18) and essentially the same number of particles, 9,712, move in the opposite direction (the blue particles in Fig. 18). The fluid easily penetrates primarily near the center of the trailing edge, where the vibration amplitude is large and the effect of the tip vortices is limited. Conversely, the fluid particles rarely permeate the flag near the leading edge, especially in the vicinity of $\xi = 0.2$. When the permeability is high at $\phi = 0.5$, the numbers of passing particles are reduced to 6,242 and 6,349, respectively, and the total number is 12,591. In this case, they permeate

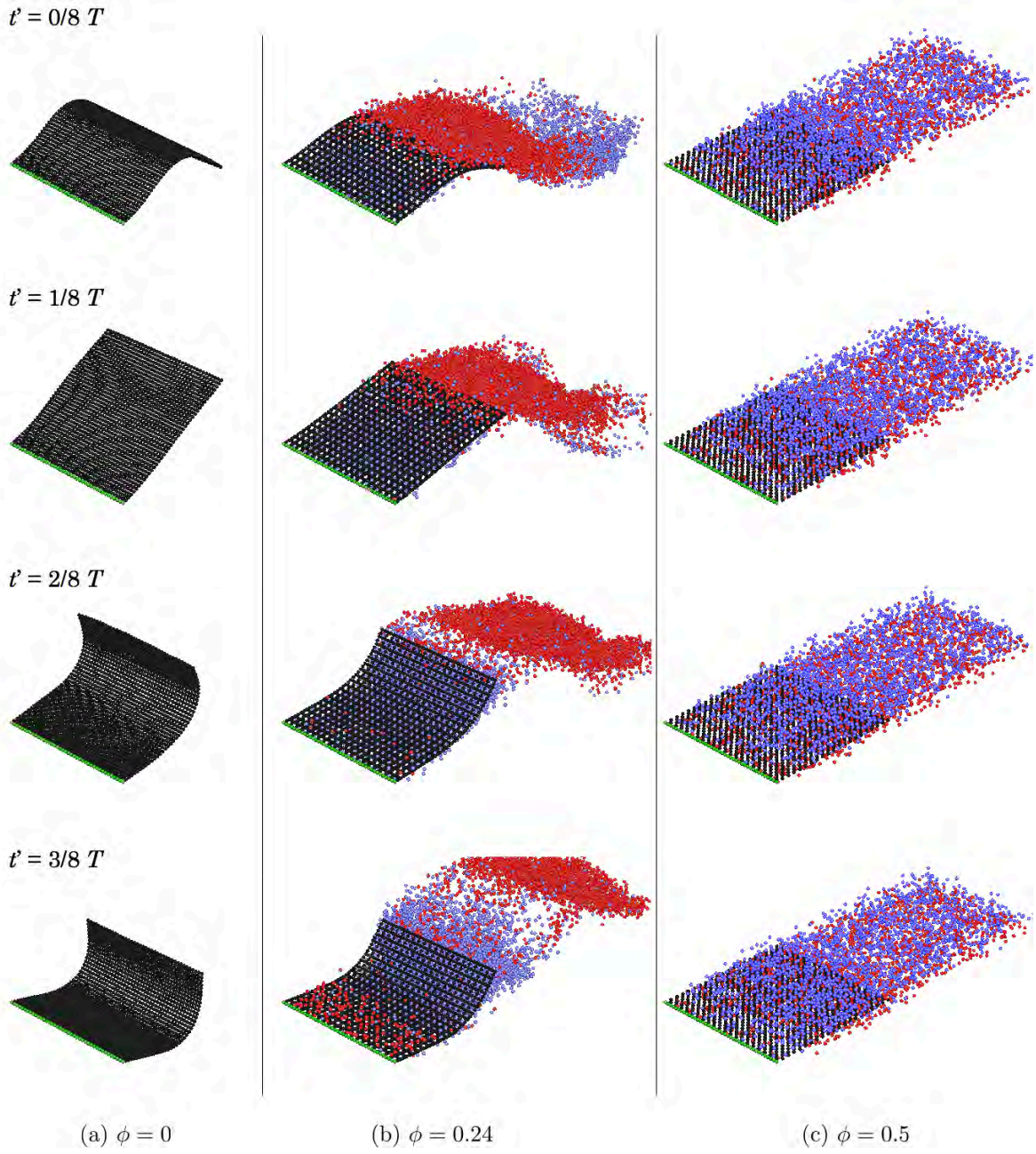

Figure 18. Visualizations of the permeated particles during a half cycle of an oscillation at $Re = 2.2 \times 10^4$ and $B^* = 2.2 \times 10^{-3}$: (a) $t^* \in [23.9,\ 26.2]$ for $\phi = 0$, (b) $t^* \in [39.5,\ 32.1]$ for $\phi = 0.24$, and (c) $t^* \in [23.9,\ 26.2]$ for $\phi = 0.5$. The red makers are particles that permeated from the upper surface to the lower surface, and the blue makers are particles that permeated in the opposite direction.

all over the flag nearly uniformly, unlike in the low-permeability case, even though the permeations are slightly more active near the leading edge. Note that, limited to the region near the leading edge at $\xi \in [0,\ 0.04]$, there is no remarkable difference in the number of permeating particles: 917 in the low-permeability case and 1,170 in the high-permeability case. This is likely related to the temporal change in the relative angle of

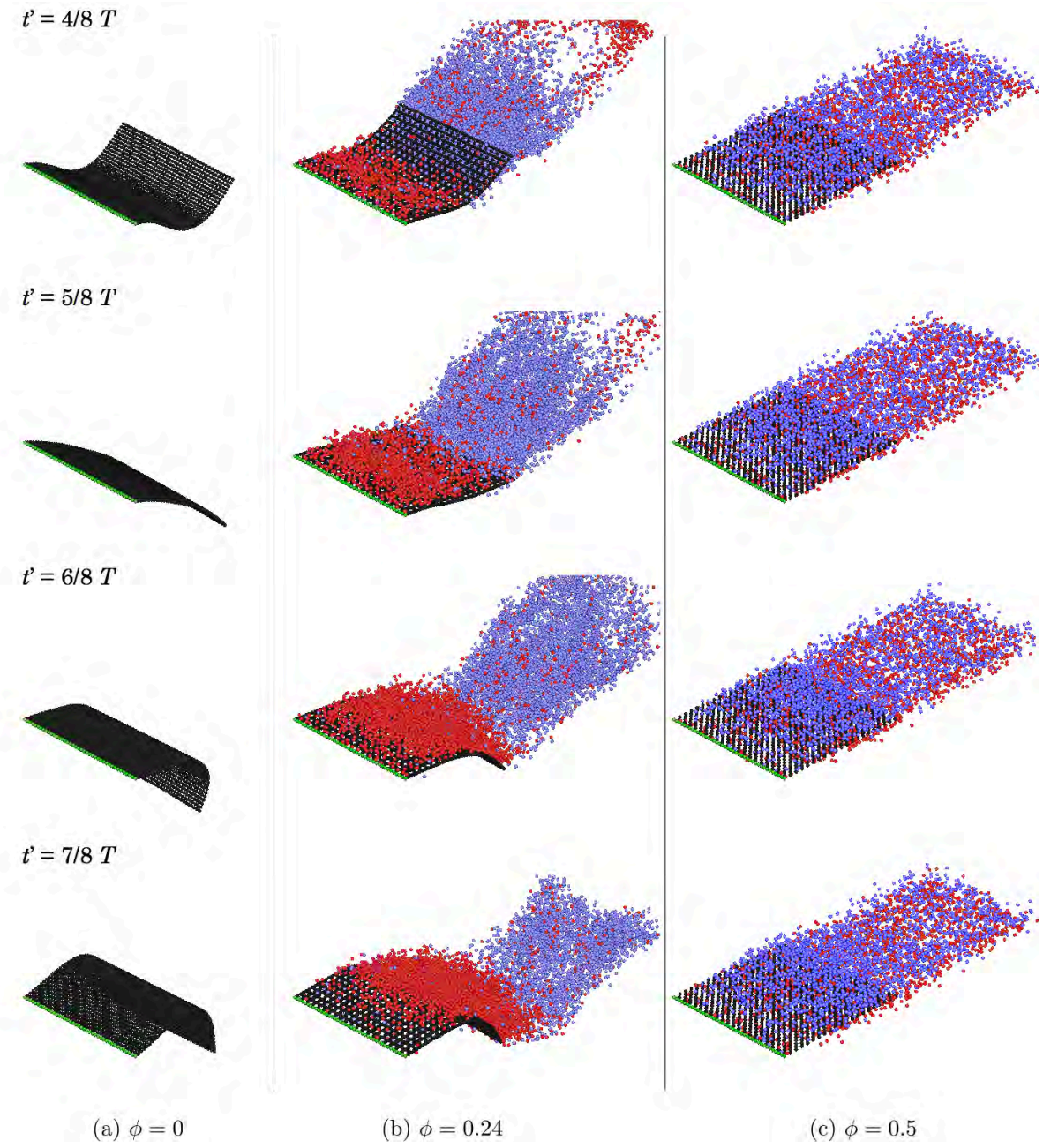

Figure 18. *Continued.*

attack accompanying the small movement of the flag.

The relationship between the number of penetrating particles and the fluid force acting on the flag surface was investigated. Figure 20 shows the distributions of the time-averaged work done by the fluid force for one cycle of oscillation, given by

$$\overline{W_{i,f}} = \frac{1}{T}\int_0^T \boldsymbol{F}_i \cdot \Delta \boldsymbol{r}_i \mathrm{d}t, \tag{17}$$

where $\boldsymbol{F}_i$ is the fluid force and $\Delta \boldsymbol{r}_i$ is the displacement vector for the flag particle i at each time step. For each case, the work is normalized by its maximum value. The low-permeable flag of $\phi = 0.24$ shows nearly the same tendency as the impermeable flag.

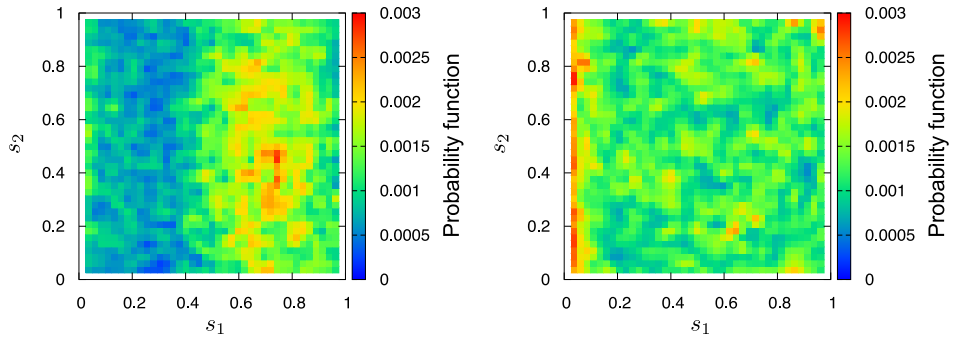

(a) $\phi = 0.24$ (b) $\phi = 0.5$

Figure 19. Probability functions of the permeating fluid particle numbers when $Re = 2.2 \times 10^4$ and $B^* = 2.2 \times 10^{-3}$.

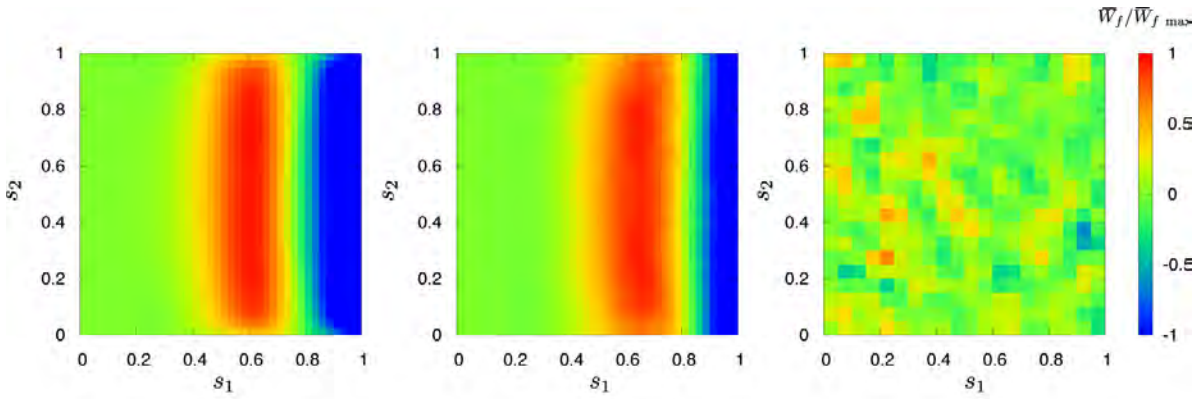

(a) $\phi = 0$ (b) $\phi = 0.24$ (c) $\phi = 0.5$

Figure 20. Distributions of the local work done by the fluid on the flag for different permeability ϕ cases when $Re = 2.2 \times 10^4$ and $B^* = 2.2 \times 10^{-3}$.

In both cases, the sign of the work becomes positive near $\xi = 0.6$ and negative near the trailing edge. A comparison of Figs. 19(a) and 20(b) indicates the location where a large number of particles permeate is close to the location where the work by the fluid on the flag is positive. This is likely due to the fluid particles being pushed through the flag by the large pressure difference between the two sides of the flag in this region.

4.4. Vortical structures

Vortical structures shed from the impermeable flag and the low-permeable flag of $\phi = 0.24$ during one cycle of oscillation are shown in Figs. 21 and 22. Here, the isosurface of the second invariant of the velocity gradient tensor, $Q = 2.0$, is used to identify the vortical structures and their surfaces are colored according to the local value of the streamwise vorticity component, ω_x^*. Tip vortices generated at the spanwise edges of both flags accompanying the vertical movement of the flags can be observed. However, they form different structures in the wake region. While the two longitudinal vortices generated from the impermeable flag are connected to the spanwise vortex shed from

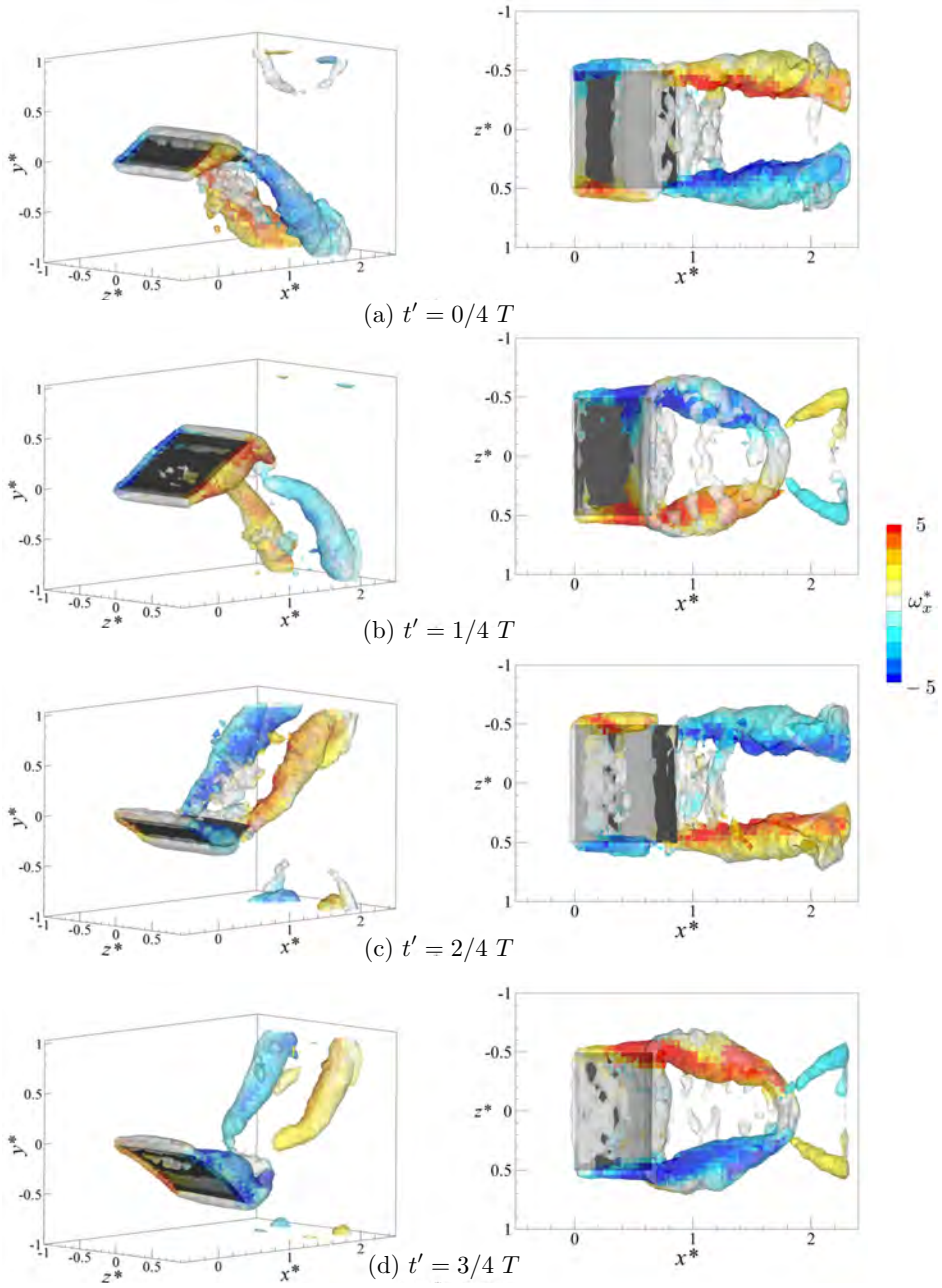

Figure 21. Vortical structures near the impermeable flag ($\phi = 0$) visualized for $Q = 2.0$ at $t' =$ (a) 0, (b) $1/4T$, (c) $2/4T$, and (d) $3/4T$.

the trailing edge forming a V-shaped vortex, such a reconnection is not observed in the permeable flag case. The longitudinal vortices appear to be weaker and are convected downstream.

Figures 23 and 24 show the vorticity fields in the x^*y^* planes at the midpoint $z^* = 0$ and in the y^*z^* planes at $x^* = 1$. $x^* = 1$ is the initial trailing edge location. The vorticity field in the x^*y^* section shows that the flag is oscillating while bending in a

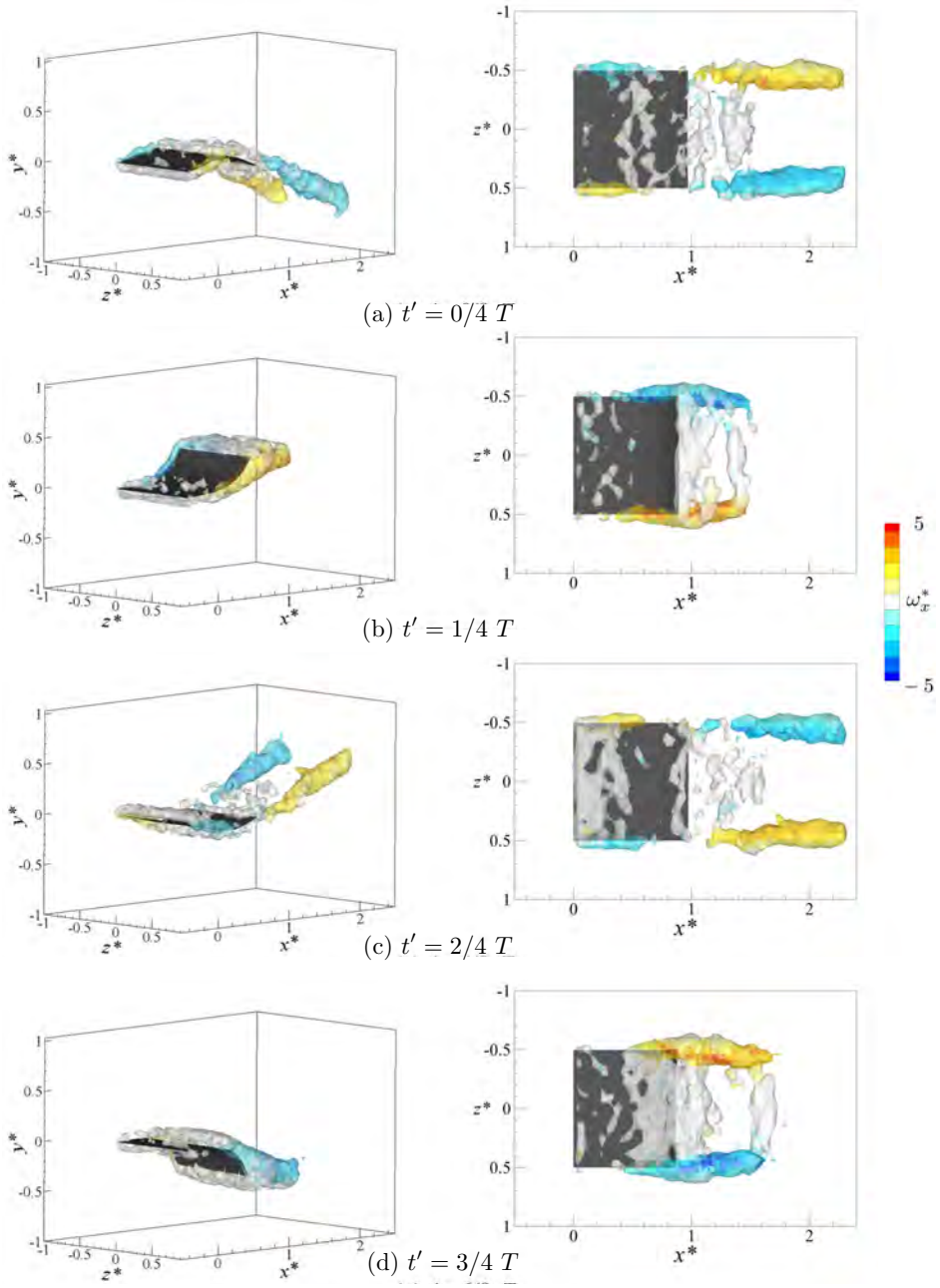

Figure 22. Vortical structures near the permeable flag for permeability $\phi = 0.24$ visualized for $Q = 2.0$ at $t' =$ (a) 0, (b) $1/4T$, (c) $2/4T$, and (d) $3/4T$ ($Re = 2.2 \times 10^4$ and $B^* = 2.2 \times 10^{-3}$).

doglegged shape. The fluid flows along the curved surface, and a large flow separation is not observed. Because the flags are made of relatively soft materials, if a low-pressure region derived from a flow separation begins to develop, the flag will be pulled in that direction. Therefore, flows around the flags may be inherently less likely to separate.

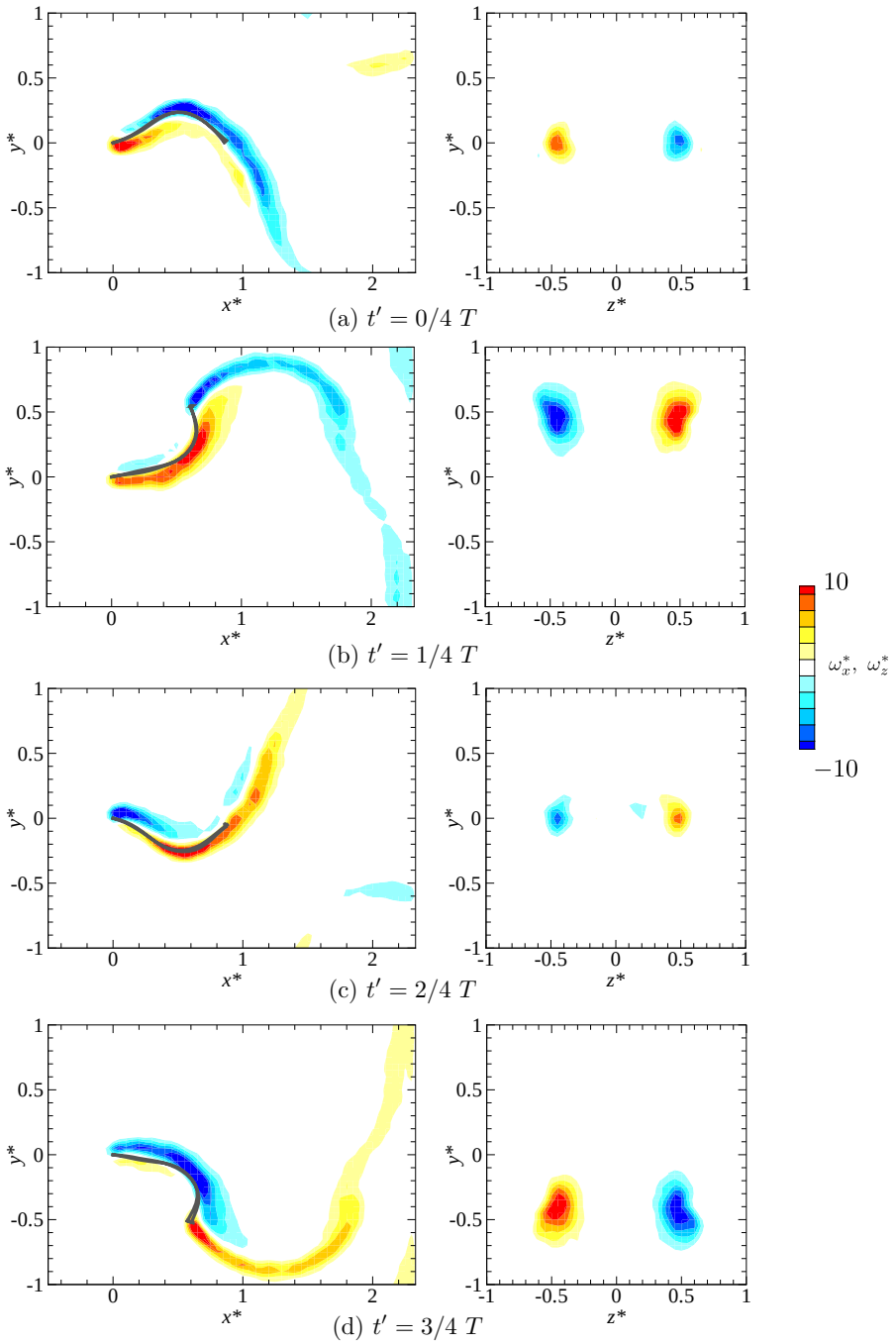

Figure 23. Vorticity fields for the impermeable flag case in (left) the $z^* = 0$ planes and (right) the $x^* = 1$ planes at $t' =$ (a) 0, (b) $1/4T$, (c) $2/4T$, and (d) $3/4T$ ($Re = 2.2 \times 10^4$ and $B^* = 2.2 \times 10^{-3}$).

The circulation of the tip vortex given by

$$\Gamma_x^* = \int_S \omega_x \mathrm{d}S \tag{18}$$

is estimated by executing the surface integral over the region of $z^* > 0$ in the $z^* y^*$ plane at $x^* = 1$. The result is shown in Fig. 25, together with the lift coefficient C_L, the drag

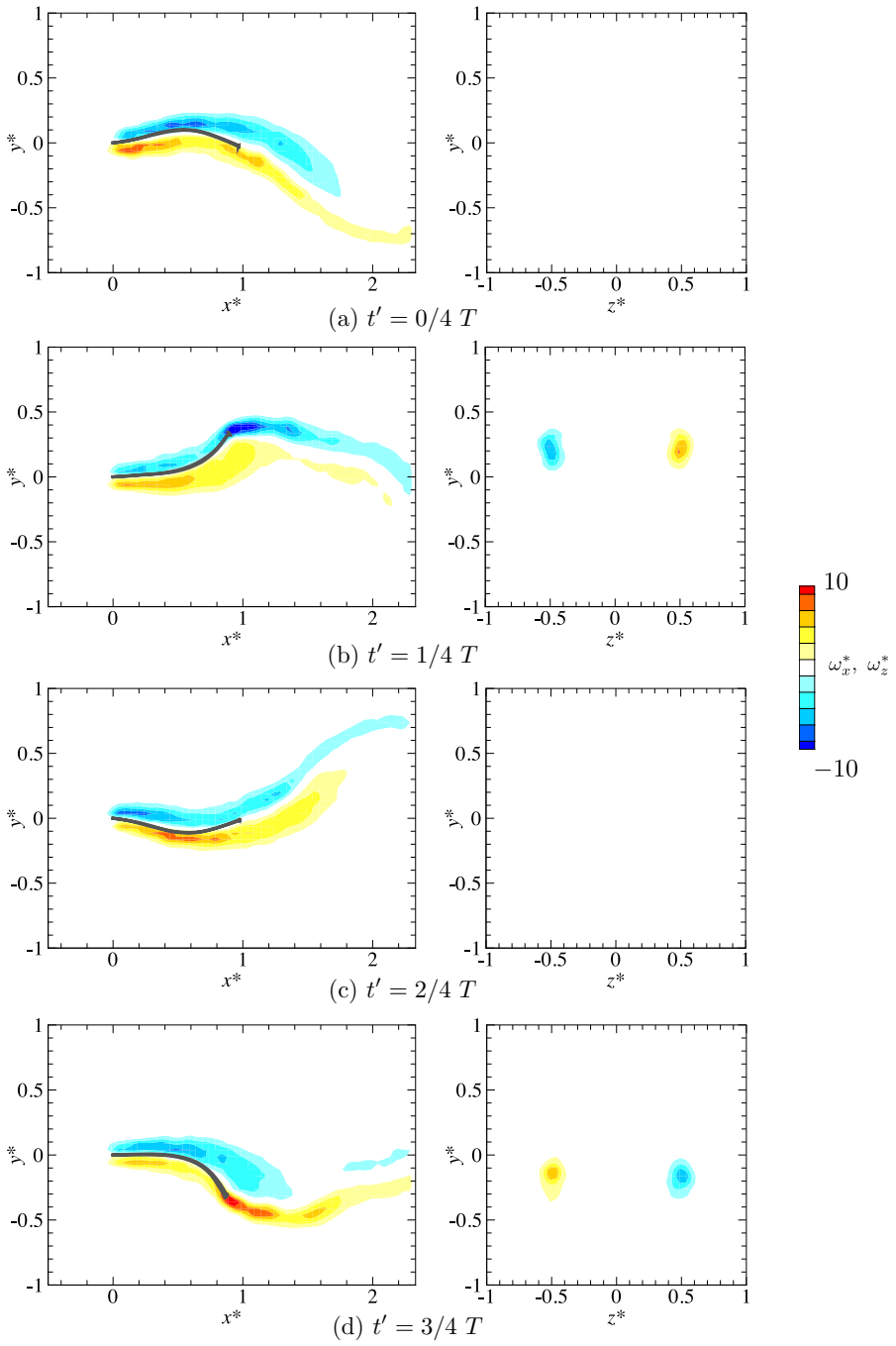

Figure 24. Vorticity fields for the $\phi = 0.24$ permeable flag case in (left) the $z^* = 0$ planes and (right) the $x^* = 1$ planes at (a) $t' = 0$, (b) $t' = 1/4T$, (c) $t' = 2/4T$, and (d) $t' = 3/4T$ ($Re = 2.2 \times 10^4$ and $B^* = 2.2 \times 10^{-3}$).

coefficient C_D, and the vertical displacement of the free end of the flag y^*. The drag force reaches a maximum when the absolute value of the vertical displacement of the free end becomes largest, which is when the flag's projected area in the z^*y^* plane becomes largest. Meanwhile, the lift force reaches maximum/minimum values and crosses zero slightly earlier than the movement of the free end of the flag. The strength of the

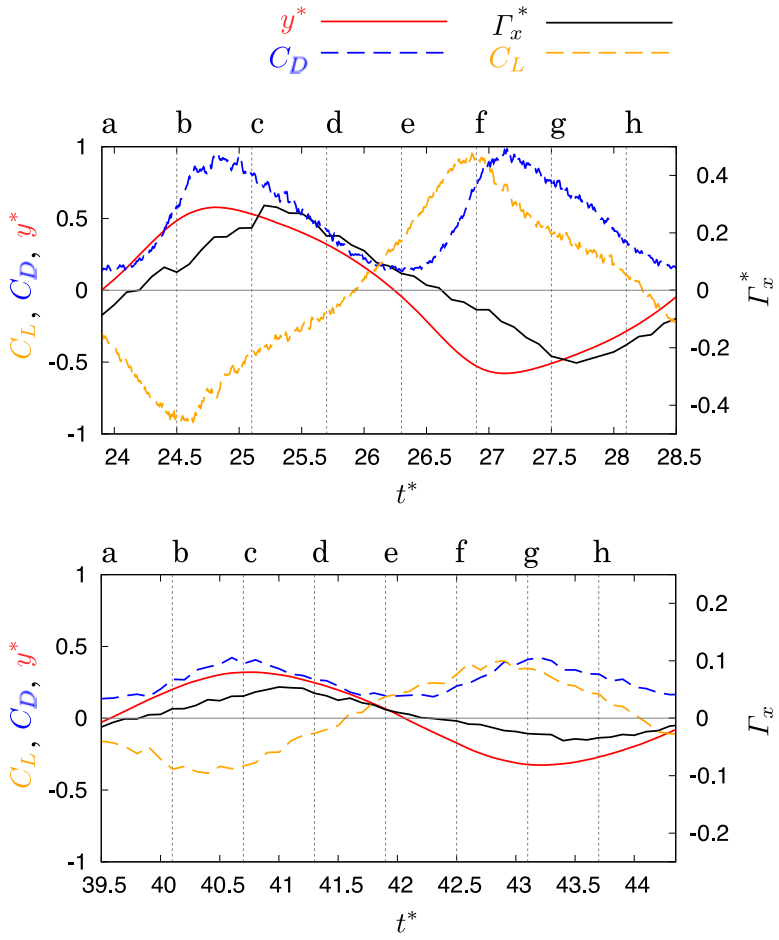

Figure 25. Time variations of the lift coefficient C_L, the drag coefficient C_D, the free-end locations y^*, and the circulation Γ_x^* for the permeability (top) $\phi = 0$ and (bottom) $\phi = 0.24$ cases when $Re = 2.2 \times 10^4$ and $B^* = 2.2 \times 10^{-3}$.

tip vortex changes along with the instantaneous lift force acting on the flag but with a small time delay. The small difference in the timing is likely derived from the undulation motion of the flag and the distance between the aerodynamic center and the trailing edge of the flag. Note that, in the case of the permeable flag of $\phi = 0.24$, the circulation of the tip vortices is reduced by half compared to the impermeable flag and so is the magnitude of the lift.

5. Conclusions

The influence of permeability on the dynamics of a flapping flag was numerically studied using the incompressible SPH method in combination with a newly proposed permeable flag model. Wind tunnel experiments were also performed, and the results were compared. The present scheme was successful in simulating the flapping behavior of the flag, and two states of the flag, namely the "stretched-straight state" and the "flapping state," which switched depending on the uniform velocity, were reproduced

in the simulation. However, the hysteresis behavior of the bistable region did not appear in the computation. The oscillation periods and the tail-end trajectories matched the experiments very well. Except for the high-permeability case, the flags oscillated two dimensionally while bending in a doglegged shape irrespective of the permeable conditions. A flow separation from the flapping flags was not observed. This might be due the flexibility of the flag in which the flag can change its shape in response to the low fluid pressure acting on its surface. In addition, a pair of longitudinal vortices rotating in opposite directions was observed at both spanwise ends of the flapping flag. The strengths of the longitudinal vortices varied in accordance with the instantaneous lift force. When the flag was impermeable, these longitudinal vortices were connected to the spanwise vortex shed from the trailing edge and deformed into a V-shaped vortex downstream. Conversely, in case of a permeable flag, the generated longitudinal vortices simply moved downstream without reconnecting. In addition, for the permeable flag, it was found that the fluid permeation took place at the location where the work by the fluid on the flag was concentrated.

References

Alben S & Shelley M 2008 *Physical Review Letters* **100**(7), 074301.

Argentina M & Mahadevan L 2005 *Proceedings of the National Academy of Sciences of the United States of America* **102**(6), 1829–1834.

Bae J, Lee J, Kim S, Ha J, Lee B, Park Y, Choong C, Kim J, Wang Z, Kim H, Park J & Chung U 2014 *Nature Communications* **5**.

Choi K & Ko H 2002 *ACM Trans. Graph.* **21**(3), 604–611.

Connell B & Yue D 2007 *Journal of Fluid Mechanics* **581**, 33–67.

Eloy C, Lagrange R, Souilliez C & Schouveiler L 2008 *Journal of Fluid Mechanics* **611**, 97–106.

Harada T, Koshizuka S & Kawaguchi Y 2007 *in* 'TPCG' pp. 13–20.

Huang W & Sung H 2010 *Journal of Fluid Mechanics* **653**, 301–336.

Ito M, Nishio Y, Izawa S, Fukunishi Y & Shigeta M 2015 *Quarterly Journal of the Japan Welding Society* **33**(2), 34s–38s.

Michelin S & Doaré D 2013 *Journal of Fluid Mechanics* **714**, 489–504.

Michelin S, Smith S & Glover B 2008 *Journal of Fluid Mechanics* **617**, 1–10.

Paidoussis M P 2014 *Fluid-structure interactions: slender structures and axial flow* Academic Press.

Rayleigh L 1878 *Proceedings of the London Mathematical Society* **s1-10**(1), 4–13.

Sawada T & Hisada T 2007 *Computers and Fluids* **36**(1), 136–146.

Shelley M & Zhang J 2011 *Annual Review of Fluid Mechanics* **43**(1), 449–465.

Tada S, Satke M, Shigeta M, Izawa S & Fukunishi Y 2011 *The Proceedings of Mechanical Engineering Congress, Japan* **2011**, G050093.

Taneda S 1968 *Journal of the Physical Society of Japan* **24**(2), 392–401.

Wilson T 1999 *Flags flown at sea by ships of the major maritime nations, from the 16th century to the present day, illustrated from the collections of the national maritime museum* National Maritime Museum.

Yamada K & Suzuki K 2005 *Journal of the Japan Society for Aeronautical and Space Sciences* **53**(613), 51–60.

Zhang J, Childress S, Libchaber A & Shelley M 2000 *Nature* **408**(6814), 835–839.

Zhao Z, Pu X, Du C, Li L, Jiang C, Hu W & Wang Z 2016 *ACS Nano* **10**(2), 1780–1787.

Zhu X, He G & Zhang X 2014 *Journal of Fluids Engineering, Transactions of the ASME* **136**(4).